Journal of CO2 Utilization 55 (2022) 101811

Contents lists available at ScienceDirect

Journal of CO2 Utilization

journal homepage: www.elsevier.com/locate/jcou

Computational insights into efficient CO_2 and H_2S capture through zirconium MOFs

Hakan Demir *, Seda Keskin *

Department of Chemical and Biological Engineering, Koc University, 34450, Istanbul, Turkey

ARTICLE INFO

Keywords:
Metal organic frameworks
Computational screening
CO_2 separation
H_2S separation
CO_2/CO
CO_2/H_2
CO_2/N_2
H_2S/CO_2
Zirconium MOFs

ABSTRACT

Separation of CO_2 involving mixtures is relevant to the various industrial settings and preserving environment for which different classes of materials including metal-organic frameworks (MOFs) have been researched. Herein, CO_2/CO, CO_2/H_2, CO_2/N_2, and H_2S/CO_2 separation properties of the zirconium MOFs are computationally investigated mimicking vacuum swing adsorption (VSA) process. Structure-performance relationships are established and the best performing adsorbent materials are determined considering three performance metrics: adsorption selectivity, working capacity, and regenerability. For CO_2/CO separation in dry conditions, PCN-59, BUT-10, and PCN-58 are identified to be the top three materials with CO_2/CO selectivities of 219.8, 47.2, and 28.6, CO_2 working capacities of 6.9, 5.3, and 4.0 mol/kg, CO_2 regenerabilities of 63.3, 82.1, and 87.2 %, successively. In humid conditions, UiO-66-OH and MOF-805 appear promising for CO_2/CO separation. Regarding CO_2/H_2 separation in dry conditions, PCN-59, BUT-10, and LIFM-94 are ranked as the top three MOFs exhibiting CO_2/H_2 selectivities of 1445.6, 378.1, and 411.3, CO_2 working capacities of 3.6, 2.4, and 2.2 mol/kg, and CO_2 regenerabilities of 56.6, 84.9, and 83.9 %, successively. These three materials are also found to be the top three materials for CO_2/N_2 separation in dry conditions with CO_2/N_2 selectivities of 346.0, 53.3, and 54.9, CO_2 working capacities of 3.6, 2.3, and 2.2 mol/kg, and CO_2 regenerabilities of 56.3, 84.1, and 83.9 %, successively. For CO_2/H_2 and CO_2/N_2 separation in humid conditions, UiO-66-NH_2 is potentially useful. Considering H_2S/CO_2 separation in dry conditions, NU-1101, PCN-58, and LMOF-1 are identified to be the best three MOFs attaining H_2S/CO_2 selectivities of 109.7, 30.9, and 90.7, H_2S working capacities of 1.6, 2.3, and 1.2 mol/kg, and H_2S regenerabilities of 43.0, 56.4, and 43.7 %, respectively. All top materials for H_2S/CO_2 separation show relatively large water affinities (PCN-57 having the smallest affinity) which might render them inefficient for H_2S/CO_2 separation in humid conditions. Adsorbate density profiles are generated for the top 3 materials to elucidate the adsorption mechanisms for each gas separation. A comparison of predictions based on PACMOF and EQeq charges demonstrates drastic differences in material rankings, and separation performance metrics.

1. Introduction

Every year, CO_2 is emitted to the atmosphere in enormous volumes as a result of fossil fuel combustion significantly contributing to the global warming [1]. One of the most researched areas to mitigate or reverse the effects of global warming is carbon capture for which energy efficient solutions including adsorption and membrane-based separation are being sought [2,3]. Carbon capture technologies are being investigated for several applications including precombustion (CO_2/H_2) [4], post-combustion CO_2 capture (CO_2/N_2) [5], and CO_2/CO separation [6].

Hydrogen is deemed as an alternative to the fossil fuels since its combustion product is water instead of polluting CO_x products [7]. As such clean combustion features are highly desirable, separating and storing H_2 at low cost would help make the societies transition from fossil fuel economy into the hydrogen economy [8]. So far, several H_2 storage paths mainly compression, liquefaction, and physisorption have been investigated among which the last one is a popular choice due to its potential energetic benefit [9]. This implies that an efficient separation of CO_2/H_2 mixture, which can be commonly found in refinery gas streams [10], would not only help mitigate the CO_2 emissions but also enable acquiring high purity H_2 streams that could subsequently be stored using porous materials. In this regard, Chung et al. [4] investigated CO_2/H_2 (20/80) separation performance of hypothetical and experimental metal-organic frameworks (MOFs) where NOTT-101/OEt

* Corresponding authors.
E-mail addresses: hakdemir@ku.edu.tr (H. Demir), skeskin@ku.edu.tr (S. Keskin).

https://doi.org/10.1016/j.jcou.2021.101811
Received 3 August 2021; Received in revised form 15 October 2021; Accepted 15 November 2021
Available online 26 November 2021
2212-9820/© 2021 The Authors. Published by Elsevier Ltd. This is an open access article under the CC BY-NC-ND license (http://creativecommons.org/licenses/by-nc-nd/4.0/).

exhibited the largest CO_2 working capacity of 3.8 mol/kg and a mediocre CO_2/H_2 selectivity of 60. Avci et al. [11,12] studied CO_2/H_2 (15/85) mixture separation performances of MOFs at room temperature using grand canonical Monte Carlo (GCMC) simulations where CO_2/H_2 selectivities are determined to be in a broad range of 2.5-10^5 for vacuum swing adsorption (VSA) condition. This implies that some of the structures identified in these large-scale screening studies are much more CO_2 selective than five MOFs [8] exhibiting CO_2/H_2 selectivities (calculated by Ideal Adsorbed Solution Theory (IAST) [13] based on experimental isotherms) in a relatively smaller range of ~2−860 approximately at 5 bar, 313 K for a CO_2/H_2 (20/80) mixture. This observation underlines the importance of performing large-scale computational screening studies as it can accelerate material discovery and help cut down experimental research cost and time.

The separation of the flue gas, mainly composed of CO_2 and N_2, is another critical field in gas separations as the volume of flue gas emitted is enormous [14]. Over the decades, the CO_2 concentration in the air has increased surpassing 400 ppm recently [15]. It is considered that the efficient CO_2/N_2 separation would help lessen the greenhouse effects caused by the CO_2 build-up in the atmosphere through subsequent CO_2 underground storage [16]. However, it is estimated that the use of carbon capture technologies would incur significant energy cost, thus, besides having optimum operating conditions, the adsorbents for CO_2/N_2 separation should possess optimal features [17]. So far, many investigations have been conducted probing CO_2 capture properties of the adsorbents [18,19]. For instance, Yu et al. [20] explored the CO_2/N_2 separation capabilities of several dry and hydrated HKUST-1 materials with different metals at various pressures, room temperature and revealed that CO_2/N_2 selectivities can vary broadly in a range of ~13−80 at 1 bar. In an experimental study of Cui et al. [21], two Cu-based MOFs are compared in terms of their CO_2/N_2 selectivities where CuBDC-NO_2-a exhibits a slightly higher CO_2/N_2 selectivity of 28 than CuBDC-Br-a (25) for a CO_2/N_2 (15/85) mixture at ambient conditions. Dai et al. [22] synthesized a Cu-based MOF, SMOF-SIFSIX-1a, which attains a CO_2/N_2 selectivity of ~60 for a CO_2/N_2 (15/85) mixture at room temperature and pressure. Boyd et al. [23] computationally screened over 300,000 structures for flue gas separation at ambient conditions where the CO_2/N_2 selectivity and CO_2 working capacity could exceed 200 and 5.0 mol/kg.

CO_2/CO mixture (along with some impurities) can be obtained as a result of several processes involving steam methane reforming, coal gasification, partial oxidation of hydrocarbons *etc.* [24] Although CO is a toxic gas which can pose health threats, when used as a reactant to produce other chemicals including alcohols, and acetic acid, it can bring about huge economic benefits [25]. Similarly, several chemicals including formic acid, methanol, dimethyl ether, and olefins can be obtained using CO_2 as a feedstock [26]. Thus, the efficient separation of CO_2/CO mixture would allow for acquiring high-purity reagents that can be used to economically generate other chemicals, contributing to the carbon cycle [27]. However, this separation could be highly energy intensive due to the similar gas properties [24]. To further the efficiency of this separation, an increasing number of studies has focused on MOFs. Mishra et al. [28] probed the CO_2/CO (20/80) separation on isostructural M/DOBDC (M = Mg, Mn, Co, and Ni) structures around the room temperature where Mg and Mn (Co, and Ni) variants are determined to be CO_2 (CO) selective at 1 bar. Similar conclusions are drawn for Mg, Co, and Ni variants of M/DOBDC by Kim et al. [29] One of the most CO_2 selective MOFs is identified by Chen et al. [30] as SIFSIX-3-Ni exhibiting a CO_2/CO selectivity of 12000 at the room temperature and pressure for an equimolar CO_2/CO mixture.

Another common gas mixture where acidic components can exist is biogas whose composition can vary broadly depending on its origin [31]. H_2S and CO_2 can be two components of biogas whose separations are crucial as they have detrimental effect on health, environment and/or infrastructure [32]. Besides, these two pollutants may be found in specific industrial streams including refinery off-gas [33]. Due to their potentially harmful effects, there are pipeline specifications limiting the concentration of CO_2 and H_2S in biogas mixture that would be fed [32]. While removing both H_2S and CO_2 from desired gases simultaneously could be desirable, owing to the complex interplay of disparate interactions of various gases in the gas mixtures, a multi-stage separation process may be needed for gases like biogas where particular undesired species are removed in different steps. For instance, HKUST-1 is reported to be more selective towards H_2S than CO_2 which might prompt removing H_2S first and handling the rest of the mixture subsequently [34]. Zhang et al.'s computational investigation [35] on a list of functionalized porous aromatic frameworks (particularly PAF-1 variants) regarding the H_2S/CO_2 separation revealed that their H_2S/CO_2 selectivities at 298 K, 1 bar are in a narrow range of 1.5–2.5 where the highest H_2S/CO_2 selectivity is obtained by the -NO_2 functionalized PAF-1. Sokhanvaran et al.'s investigation [36] on pristine MIL-47, MIL-47-OH, and MIL-47-OCH_3 demonstrated that the H_2S/CO_2 selectivity of them follow the order of MIL-47-OCH_3 (6) > MIL-47-OH (4) ~ MIL-47 (4) at ambient temperature and pressure. Bhatt et al. [37] reported H_2S/CO_2 selectivities of three rare earth fcu-MOFs at ambient conditions which range between 4 and 6.4.

The foregoing examples illustrate that the MOFs could potentially have widespread use, however, the relatively low stability of some MOFs may hinder their use in industry [38]. It has been demonstrated that high-valent metals tend to form thermally, hydrothermally stable structures in different environments (*i.e.*, acidic and basic) enabling their potential use in practical applications [39,40]. Specifically, Zr-MOFs garnered much interest as they showed success in various gas storage/separation applications encouraging their experimental and computational investigation [41]. Although the number of studies on synthesized Zr-MOFs is increasing at a high pace, the reported structures may involve structural problems such as lacking atoms, presence of disorder, lack of optimization *etc* [42–44]. Since the adsorption properties are influenced by the accuracy of the atomic structures, curation of structures is important as shown earlier [45]. Recently, Zhou et al. [46] curated Zr-MOFs by removing disorder, determining energetically favorable proton topologies, adding hydrogens, and optimizing structures which facilitates obtaining accurate computational results regarding their gas separation potentials.

To explore the CO_2 and H_2S capture potentials of the Zr-MOFs at room temperature, herein, four gas mixtures, CO_2/CO, CO_2/H_2, CO_2/N_2, and H_2S/CO_2, are studied using GCMC simulations from which structure-performance relationships and the best performing adsorbent materials are determined. Besides, the most preferred adsorption sites are exhibited in sorbate density profiles for the top 3 materials which elucidate the adsorption mechanisms. It is worthwhile to note that although the MOFs are evaluated as adsorbents in this work, their potential use is not limited to adsorbents as they can be used as membranes, too. However, as the diffusional properties of the structures directly affect the separation performances of the membranes, a good adsorbent may not necessarily serve as a good membrane, especially if the window/pore sizes are comparable with the sorbate sizes limiting the diffusion [47].

2. Computational methods

To study the separation of CO_2/CO (50/50), CO_2/N_2 (15/85), CO_2/H_2 (15/85), and H_2S/CO_2 (2/98) gas mixtures at 298 K, GCMC simulations are carried out in RASPA [48] using 10,000 (10,000), 10,000 (10,000), 50,000 (50,000), and 50,000 (50,000) equilibration (production) cycles, respectively. The adsorption and desorption pressures are selected as 1 and 0.1 bar, successively, resembling vacuum swing adsorption (VSA) operation. Molecules are allowed to have the moves of insertion/deletion, translation, rotation (except H_2), and identity change with equal probabilities. The molecule interaction parameters are acquired from earlier works [49–52]. MOF atom interactions are described using Universal Force Field (UFF) [53] parameters and MOFs

are assigned partial atomic charges in metal–organic frameworks (PACMOF) [54] and extended charge equilibration (EQeq) [55] charges, separately. PACMOF charges are based on a machine-learning model fitted to density derived electrostatic and chemical (DDEC) charges [56–62] while EQeq charges rely on the ionization potential and electron affinity of the atoms [54,55]. Lennard-Jones interactions are truncated at 12 Å and Lorentz-Berthelot mixing rules are employed to acquire cross-interaction terms. Electrostatic interactions are calculated through Ewald summation [63]. The pore characteristics (*i.e.*, GCD: Global Cavity Diameter, PLD: Pore Limiting Diameter, LCD: Largest Cavity Diameter, SA: Surface Area, V_f: Void Fraction, V_p: Pore Volume) are determined using Zeo++ [64] with a probe radius of 1.84 Å. The inaccessible regions in the porous space are blocked by inserting spheres having radii slightly smaller (0.1 Å) than the molecular radii of gases to consider structural flexibility/deformation.

Three performance metrics are used to analyze the gas separation performance of the MOFs – adsorption selectivity, working capacity, and regenerability. The adsorption selectivity of the first gas species over the second, $S_{ads,1/2} = \frac{N_1/N_2}{y_1/y_2}$ where N and y represent the gas uptake of the MOF and mole fraction of the gas component in the mixture, successively. Working capacity is defined as $\Delta N_1 = N_{ads,1} - N_{des,1}$ in which the first term and second term on the right-hand side correspond to the adsorption amounts at the adsorption and desorption conditions, respectively. The mathematical expression for the regenerability is $R = \frac{\Delta N_1}{N_{ads,1}}$. All these metrics play significant role in determining the cost and separation effectiveness of the gas separation operation as the adsorption selectivity indicates the extent of preferential adsorption, working capacity is a hypothetical deliverable amount of a sorbate at the desorption pressure, and regenerability defines the extent of vacating the structure as the pressure changes from the adsorption to the desorption pressure. It has been reported earlier that the presence of water can improve/worsen the desired gas uptakes/selectivities of MOFs [65,66]. The gas separation performance enhancement/deterioration due to the presence of water in a gas mixture can be elucidated fully through computationally-expensive simulations and/or experiments. As performing a full-fledged simulation for water effects is beyond the scope of our work, we pointed out the MOFs that can be potentially affected by the water presence through previously calculated heat of adsorption of water in MOFs at infinite dilution using 10^7 Widom insertions at 298 K [67].

We also compare the separation performance metrics using two different charge assignment methods in molecular simulations with the aim of finding out whether the scope of disparities in the material rankings is significant. It has been shown earlier that PACMOF charges can be at a similar quality of DDEC [54]. As it is a very recently developed method, many of the earlier studies adopted charge assignment methods based on experimental inputs [68] such as Qeq [69] and EQeq [55] whose use for the prediction of adsorption isotherms/selectivity could result in significant differences compared to experimental results or those based on density functional theory (DFT)-based charge partitioning methods [54,55,70]. However, as our recent work [67] shows there can also be cases where the material rankings could be very similar when PACMOF and EQeq charges are used.

3. Results & discussion

Zr-MOF database [46] is a collection of 182 curated structures (161, 4, and 17 structures with 12, 11, and 10-coordinated inorganic nodes) involving various functional groups (-Br, -CF_3, -CH_3, -Cl, -CN, -*COOH*, -F, -I, -NH_2, -NO_2, -OCH_3, -OH, -*SO_3H*, -SH, -*SCH_3*, -CH_2N_3, -C = O, -C≡CH *etc.*) that we filtered based on their PLD values so that both gas molecules can travel through the pores of MOFs (full details on the inorganic nodes, organic ligands, topologies and functional groups can be found in the study of Zhou et al. [46]). Moreover, structures with partial occupancies are removed as they would require larger simulation cells or multiple simulation cells to represent partial occupancies. Not to potentially experience the inadequateness of generic force fields about open metal site interactions [71], Zr-MOFs with open metal sites are also excluded. The resulting list of materials (128, 138, 128, and 129 structures) having functional groups mentioned above (except those in italics) are employed in the GCMC simulations to investigate their potentials in the separation of CO_2/CO (50/50), CO_2/H_2 (15/85), CO_2/N_2 (15/85), and H_2S/CO_2 (2/98) mixtures. The distribution of their textural properties is shown in Fig. S1. While some MOFs can be moderately-highly flexible [72,73], all structures are modeled rigid throughout the simulations as the goal of this work is to obtain a shortlist of materials from a large number of structures using computationally efficient methods to foster further studies on a selected list of materials. It has been shown earlier that the difference between the gas adsorption predictions based on flexible and rigid models can be limited especially when the pore sizes are bigger than sorbate sizes [74]. The discussion that follows elaborates on the adsorption/separation performance metrics of selected Zr-MOFs, the top materials identified based on them, and the effect of charge partitioning methods on the calculated separation performance metrics and MOF rankings.

3.1. CO_2/CO separation

Fig. 1 illustrates Zr-MOFs' CO_2/CO separation performance metrics at 298 K along with their structural features and $-\Delta H^{\circ}_{H_2O}$ values. In the left panel, all three performance metrics are shown together where the materials should ideally be located at the top right of the graph represented with dark colored circles. The semi-log $S_{CO2/CO}$ *vs.* ΔN_{CO2} data resembles a logarithmic shape (while $S_{CO2/CO}$ *vs.* ΔN_{CO2} data would demonstrate an exponential shape). In general, the shape of this relation relies on several factors including but not limited to material space, atomic charges, and adsorption and desorption conditions. For instance, there can be regions where selectivity and working capacity are inversely correlated. Such cases are typically seen in the screening of thousands of materials where there are some materials with excessively large selectivities and relatively small working capacities. [11,75] However, in this study, the number of materials screened is at least one order of magnitude less and an inverse relation between S and ΔN is not observed. Looking into specific examples, one Zr-MOF, PCN-59 (top material for CO_2/CO separation), stands out from the rest of the materials with its highest CO_2/CO selectivity of 219.8 and CO_2 working capacity of 6.9 mol/kg. The exceptional selectivity of PCN-59 stems mainly from much stronger interactions between CO_2 and the framework in comparison with the weak interactions of CO that is not seen at similar extent in the second top material, BUT-10 (see Fig. S2). Yet, PCN-59 is deficient in regenerability as it exhibits the lowest CO_2 regenerability of 63.3 %. Considering the large ΔN_{CO2} and moderate R_{CO2} of PCN-59, it can be deduced that while $N_{ads,CO2}$ is large, $N_{des,CO2}$ is also relatively high due to the strong gas adsorption at the desorption condition. Fig. S2 demonstrates that the interactions between CO_2 and the framework are dominant at both adsorption and desorption conditions revealing the main reason behind high $N_{ads,CO2}$ and $N_{des,CO2}$, thus, relatively low R_{CO2}). In contrast, the rest of the materials are highly regenerable with values between 74.8 and 90.3 %. However, a great majority of them (99 MOFs among 128) demonstrates comparatively low CO_2/CO adsorption selectivities (<10) and CO_2 working capacities (<2 mol/kg) signifying the clear trade-off between the regenerability and other two separation performance metrics. In the middle panel, many of the MOFs with high void fractions (>0.7) attain limited CO_2 working capacities (<2 mol/kg) as they have relatively weak adsorption at the adsorption pressure (1 bar). In contrast, the largest CO_2 working capacities (>2 mol/kg) are acquired by Zr-MOFs with small-medium void fractions (0.345−0.627). While as a general material design strategy, highly porous structures may be warranted for high working capacities, the relation between porosity and working capacity may be more complex than it is expected, as seen here. It is known that the gas

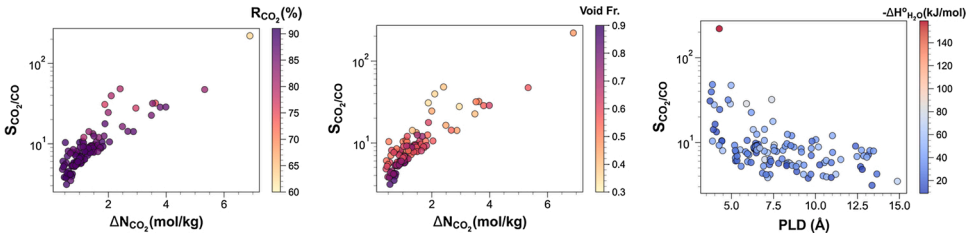


Fig. 1. CO_2/CO separation performance metrics along with the void fractions, PLDs and $\Delta H^{\circ}_{H_2O}$ of the Zr-MOFs.

separation performances of materials can be affected by the presence of water in gas mixtures. To understand which MOFs could have different gas separation performances than predicted here, the water affinities of the MOFs are estimated using the heats of adsorption of water at infinite dilution at 298 K. The right panel illustrates that the water affinities of the MOFs span a wide range, the heats of adsorption of water change from 9.4 to 159.5 kJ/mol. Among the top 10 CO_2 selective (over CO) Zr-MOFs, PCN-59 has by far the largest H_2O affinity with a $-\Delta H^{\circ}_{H_2O}$ value of 159.5 kJ/mol. However, amongst the same top 10 list, there are also MOFs with much lower water affinities such as MOF-805, UiO-66-OH, UiO-66-NH_2, and UiO-66-CH_3 having $-\Delta H^{\circ}_{H_2O}$ of 31.6, 29.6, 22.4, and 14.7 kJ/mol, respectively, and the gas separation performance of these MOFs would be less affected by the presence of water in the gas mixture.

The left panel of Fig. S3 demonstrates an inverse relationship between the CO_2/CO selectivity and PLD of the Zr-MOFs. The highest CO_2/CO selectivities (>20) are exhibited by MOFs with very narrow PLDs (<6 Å) whereas selectivities drop dramatically as the pore sizes expand. For example, PCN-230 with the largest PLD of 14.88 Å attains one of the lowest CO_2/CO selectivities of 3.5 as the confinement effects are weaker in its highly porous network (void fraction of 0.877, pore volume of 4.644 cm^3/g). Since the electrostatic interactions play a considerable role in the adsorption of both sorbates, using geometric properties namely PLD as the only descriptor could lead to a list of materials some of which may not be the most selective structures as evidenced by Zr_6-fBPDC with a very narrow PLD of 3.87 Å attaining a mediocre CO_2/CO selectivity of 10.4. A similar conclusion can be drawn from the right panel of Fig. S3 depicting the relation between CO_2/CO selectivity and surface area of the MOFs where dissimilar selectivities can be observed in MOFs with surface areas ~2000 and ~3000 m^2/g. However, in general, selectivities diminish as the surface areas increase. For instance, PCN-230 with the largest surface area of 6807.5 m^2/g is one of the least CO_2 selective (3.5) MOFs.

While many of the studies in the literature rank the adsorbents by the adsorption selectivity, there are more than one separation performance metric that determine adsorbents' cost effectiveness in a real separation process [76]. Herein, the best materials are determined using the overall separation performance scores which are calculated by summing up the individual separation performance scores ($Score_{X,i} = \frac{X_i}{X_{max}} \times 100$) where X_i and X_{max} designate the value of the individual performance metric X for the material i and the largest value of the individual performance metric X among all MOFs. The 10 best-performing Zr-MOFs (according to overall separation performance score) for the CO_2/CO separation are tabulated in Table 1 with their separation performance metrics and structural features. These MOFs span PLD, surface area, void fraction, and pore volume ranges of 3.87–7.39 Å, 872.9-3535.7 m^2/g, 0.393−0.627, and 0.303-1.047 cm^3/g, successively, achieving CO_2/CO selectivities of 14.2–219.8, CO_2 working capacities of 2.4–6.9 mol/kg, and CO_2 regenerabilities of 63.3–87.7 %. Amongst them, the top three Zr-MOFs are PCN-59, BUT-10, and PCN-58 with CO_2/CO_2 selectivities of 219.8, 47.2, and 28.6, CO_2 working capacities of 6.9, 5.3, and 4.0 mol/kg, and CO_2 regenerabilities of 63.3, 82.1, and 87.2 %, in respective order. The most distinct CO_2/CO selectivity (219.8) belongs to PCN-59, however, due to its strongest adsorption observed at low pressure (4.0 mol/kg of CO_2 adsorption at 0.1 bar), it is only moderately regenerable (63.3 %). Yet, as it still exhibits the largest CO_2 working capacity of 6.9 mol/kg among all Zr-MOFs, it ranks 1st overall. The top 10 ranked MOFs for CO_2/CO separation have water heats of adsorption in the range of 29.6–159.5 kJ/mol where those in the lower end of the spectrum (UiO-66-OH and MOF-805) are expected to be less affected by the water presence in the mixture.

Fig. 2 depicts the normalized (across all materials) adsorption/separation features, listed in columns, of the 10 best performing Zr-MOFs for the CO_2/CO separation. PCN-59 is the only Zr-MOF which adsorbs CO_2 very strongly both at adsorption and desorption conditions which is followed by BUT-10 and LIFM-94 having stronger CO_2 affinities than the remaining 7 structures. Another advantage of PCN-59 is its relatively low CO adsorption at both adsorption and desorption conditions resulting in its unparalleled CO_2/CO selectivity that cannot be approached by any other Zr-MOF. While BUT-10 and LIFM-94 can adsorb 45–60 % of the CO_2 adsorbed by PCN-59, their stronger CO affinities (uptakes being three folds of PCN-59) render their CO_2/CO selectivities much lower than that of PCN-59. Among the top 10 materials for the CO_2/CO separation, the CO uptakes of BUT-67 and LIFM-92 are the highest two (second and third highest) at the adsorption (desorption) conditions. Combining these high affinities towards CO with relatively low CO_2 adsorption amounts, BUT-67 and LIFM-92 can achieve CO_2/CO selectivities that are only ~6 % of PCN-59. It can be noticed that UiO-66-OH has similar CO uptakes to PCN-59, however, since its CO_2 affinity is much lower than PCN-59, its CO_2/CO selectivity is only about 20 % of

Table 1
Top 10 Zr-MOFs identified (using PACMOF charges) for the separation of CO_2/CO along with their structural properties.

Structure	SCO_2/CO	ΔNCO_2 (mol/kg)	RCO_2 (%)	GCD (Å)	PLD (Å)	LCD (Å)	SA (m^2/g)	V_f	V_p (cm^3/g)
PCN-59 [77]	219.8	6.9	63.3	14.50	4.28	14.50	2243.6	0.469	0.652
BUT-10 [78,79]	47.2	5.3	82.1	9.55	4.98	9.55	2452.5	0.581	0.679
PCN-58 [77]	28.6	4.0	87.2	12.65	5.89	12.65	3535.7	0.627	1.047
BUT-11 [78]	28.5	3.8	86.6	10.25	4.93	10.25	2026.8	0.558	0.616
MOF-805 [80]	31.7	3.5	83.6	9.23	4.80	9.23	1677.5	0.507	0.489
BUT-66 [81]	22.6	3.5	85.1	6.98	6.18	6.98	1311.7	0.406	0.387
LIFM-94 [82]	32.0	3.6	74.8	8.29	7.39	8.29	2190.9	0.507	0.608
BUT-67 [81]	14.2	2.9	87.7	7.96	6.29	7.90	1708.7	0.461	0.501
UiO-66-OH [83]	48.2	2.4	79.7	7.65	3.87	7.65	872.9	0.393	0.303
LIFM-92 [82]	14.3	2.7	86.8	7.97	6.97	7.97	2761.6	0.550	0.689



Fig. 2. Normalized adsorption/separation characteristics of the top 10 Zr-MOFs regarding the CO_2/CO separation. (In each column, normalization is across all materials.).

PCN-59 greatly affecting its ranking.

In Fig. S4, we compare the gas uptakes, and separation performance metrics of Zr-MOFs obtained using PACMOF and EQeq charges to reveal possible extents of differences in material performances. The top left panel portrays the larger extents of disparities in CO_2 uptakes in comparison with CO uptakes. In the top right panel, a scattering of data points can be seen representing differences in CO_2 working capacities. The largest difference in CO_2 working capacities belongs to PCN-59 exhibiting CO_2 working capacities of 6.9 and 1.0 mol/kg based on PACMOF and EQeq charges, successively. Examining the bottom left panel, it can be observed that many of the CO_2/CO selectivities determined using PACMOF and EQeq charges are located near the parity line whereas some of them considerably divert away from the parity line. For example, LIFM-33 exhibiting a CO_2/CO selectivity of 38.5 based on EQeq charges can attain a noticeably smaller CO_2/CO selectivity of 10.3 based on PACMOF charges. While such examples show higher CO_2/CO selectivities when EQeq charges are used, there are also counter examples as exemplified by PCN-59 demonstrating CO_2/CO selectivities of 219.8 and 7.9 based on PACMOF and EQeq charges, respectively. As the bottom right panel demonstrates, most of the highly CO_2 regenerable structures can be found near the parity line. Yet, there are a few outliers showing considerable differences in CO_2 regenerabilities based on PACMOF and EQeq charges. For example, PCN-59 possessing a high CO_2 regenerability of 83.3 % based on EQeq charges can acquire a much lower CO_2 regenerability of 63.3 % based on PACMOF charges.

3.2. CO_2/H_2 separation

Fig. 3 displays the relations between the CO_2/H_2 separation performance metrics, the structural features of the MOFs, and $-\Delta H^{\circ}_{H_2O}$ values. The left panel exhibits the exponential increase in CO_2/H_2 selectivity with respect to the CO_2 working capacity. Among all Zr-MOFs, PCN-59 appears as a distinct structure with its highest CO_2/H_2 selectivity of 1445.6 and CO_2 working capacity of 3.6 mol/kg. Yet, it suffers from its lowest CO_2 regenerability of 56.6 %. In contrast, the rest of the Zr-MOFs show very high CO_2 regenerabilities (>80 %), however, their CO_2/H_2 selectivities (6.8–485.9) and CO_2 working capacities (0.1–2.4 mol/kg) are considerably less. In the middle panel, the highly porous structures (void fraction>0.7) are confined to the relatively low CO_2/H_2 selectivity (<61) and CO_2 working capacity (<0.8 mol/kg) region. The most CO_2 selective (over H_2) MOFs (CO_2/H_2 selectivity of 190.7–1445.6) possess medium-high void fractions (0.264−0.581). While the least CO_2 selective Zr-MOF, nitro-MOF, possesses a very high void fraction of 0.865, the most CO_2 selective Zr-MOF, PCN-59, has a denser structure with a void fraction of 0.469. The right panel demonstrates that $-\Delta H^{\circ}_{H_2O}$ values can vary broadly across the 10 most CO_2 selective (over H_2) MOFs (14.7–159.5 kJ/mol). For instance, while PCN-59 shows the largest water affinity, UiO-66-Br and UiO-66-CH_3 have about one order of magnitude smaller heats of adsorption (~15 kJ/mol).

The left panel of Fig. S5 demonstrates the clear inverse relation between CO_2/H_2 selectivity and PLD as the dispersion effects diminish with the increasing PLD values. Not surprisingly, the least CO_2 selective (over H_2) MOFs are located at large PLD values among which PCN-230 with the largest PLD of 14.88 Å and void fraction of 0.877 exhibits one of the lowest CO_2/H_2 selectivity of 8.8. On the other hand, the most CO_2 selective (over H_2) Zr-MOF, PCN-59, possesses one of the smallest PLDs of 4.28 Å. Although there is a general trend of obtaining high selectivity values at small PLD values, there are exceptions like Zr_6-fBPDC with a PLD of 3.87 Å attaining a mediocre CO_2/H_2 selectivity of 34.5. Similar to the selectivity *vs*. PLD relation, there is an inverse relation between the CO_2/H_2 selectivity and surface area of the Zr-MOFs implying that MOFs with more open surfaces would be less desirable for applications requiring high selectivities. For example, PCN-230 with the largest surface area of 6807.5 m^2/g exhibits the second lowest CO_2/H_2 selectivity of 8.8. On the other hand, the highest CO_2/H_2 selectivity of 1445.6 is seen at a surface area of 2243.6 m^2/g corresponding to PCN-59 below which many other MOFs with lower selectivities can be found.

Table 2 lists the top 10 Zr-MOFs determined for the CO_2/H_2 separation along with their pore characteristics. They possess PLDs of 3.56–7.39 Å, surface areas of 705.4-2452.5 m^2/g, void fractions of 0.297−0.581, and pore volumes of 0.206−0.679 cm^3/g and exhibit CO_2/H_2 selectivities of 221.9–1445.6, CO_2 working capacities of 0.9–3.6 mol/kg, and CO_2 regenerabilities of 56.6–89.0 %. The three top-performing Zr-MOFs for the CO_2/H_2 separation are PCN-59, BUT-10, and LIFM-94 with CO_2/H_2 selectivities of 1445.6, 378.1, and 411.3, CO_2 working capacities of 3.6, 2.4, and 2.2 mol/kg, and CO_2 regenerabilities of 56.6, 84.9, and 83.9 %, respectively. While their surface areas (2243.6, 2452.5, and 2190.9 m^2/g), void fractions (0.469, 0.581, and 0.507), and pore volumes (0.652, 0.679, and 0.608) are similar, their pore sizes (*i.e.*, GCD, PLD, LCD) are dissimilar ranging between ~4−15 Å. Among the top 10 MOFs identified for the CO_2/H_2 separation, UiO-66-NH_2 possesses the least water affinity with a $-\Delta H^{\circ}_{H_2O}$ of 22.4 kJ/mol.

Fig. 4 illustrates the normalized CO_2/H_2 adsorption/separation metrics (across all materials) of the 10 top-performing Zr-MOFs. The first three ranked MOFs are predicted to capture the highest amounts of CO_2 at adsorption and desorption conditions, yet the CO_2 uptake of PCN-59 is several folds larger than other structures. Although strong

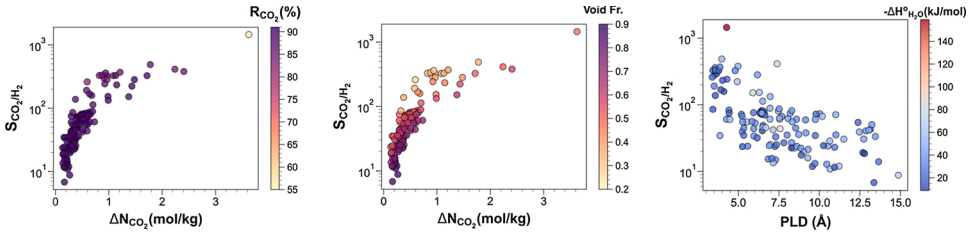


Fig. 3. CO_2/H_2 separation performance metrics together with the void fractions, PLDs, and $\Delta H^{\circ}_{H_2O}$ of the Zr-MOFs.

Table 2
10 top-performing Zr-MOFs identified (using PACMOF charges) for the separation of CO_2/H_2 in tandem with their structural features.

Structure	SCO_2/H_2	ΔNCO_2 (mol/kg)	RCO_2 (%)	GCD (Å)	PLD (Å)	LCD (Å)	SA (m^2/g)	V_f	V_p (cm^3/g)
PCN-59 [77]	1445.6	3.6	56.6	14.50	4.28	14.50	2243.6	0.469	0.652
BUT-10 [78,79]	378.1	2.4	84.9	9.55	4.98	9.55	2452.5	0.581	0.679
LIFM-94 [82]	411.3	2.2	83.9	8.29	7.39	8.29	2190.9	0.507	0.608
MOF-812 [80]	485.9	1.8	85.4	5.80	3.97	5.79	939.8	0.345	0.294
MOF-805 [80]	324.7	1.7	88.8	9.23	4.80	9.23	1677.5	0.507	0.489
BUT-66 [81]	281.1	1.5	89.0	6.98	6.18	6.98	1311.7	0.406	0.387
BUT-11 [78]	221.9	1.4	88.8	10.25	4.93	10.25	2026.8	0.558	0.616
UiO-66-OH [83]	367.5	1.2	85.1	7.65	3.87	7.65	872.9	0.393	0.303
UiO-66-NH_2 [84]	327.3	1.1	86.8	7.64	3.80	7.64	828.2	0.365	0.285
MOF-802 [80]	358.8	0.9	86.2	5.99	3.56	5.98	705.4	0.297	0.206

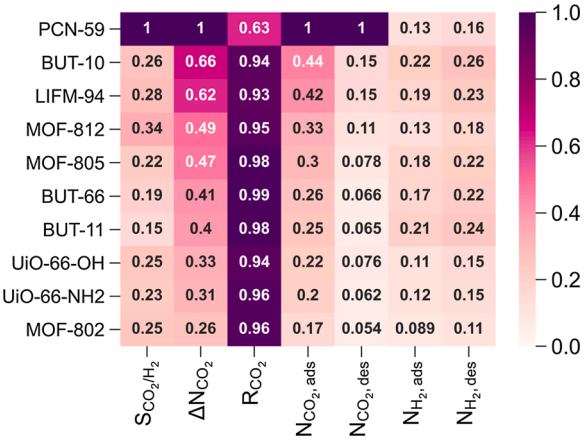


Fig. 4. Normalized adsorption/separation characteristics of the top 10 Zr-MOFs regarding the CO_2/H_2 separation. (In each column, normalization is across all materials.).

adsorption at low pressures is a drawback for regeneration, PCN-59 has the benefit of having the highest CO_2 working capacity which is one of the reasons of being ranked as the top material. The rest of the materials in the top 10 list demonstrates weaker CO_2 affinities which, in turn, results in medium CO_2 working capacities and high CO_2 regenerabilities paving their way into the material shortlist albeit comparatively low CO_2/H_2 selectivity. While the H_2 adsorption amounts of all 10 MOFs are comparable to each other, BUT-10 and BUT-11 exhibit the largest H_2 uptakes at both adsorption and desorption conditions. Since the H_2 adsorption loadings are not minimized in any of the structures ranking 2nd-10th, they cannot achieve CO_2/H_2 selectivities relatively close to that of PCN-59.

Fig. S6 demonstrates the comparisons of gas uptakes, CO_2 working capacities, CO_2/H_2 adsorption selectivities, and CO_2 regenerabilities for CO_2/H_2 separation as determined using PACMOF and EQeq charges. The top left panel hints that the loadings of weaker interacting sorbate, H_2, are similar whereas there are bigger differences in CO_2 uptakes based on PACMOF and EQeq charges. The top right panel exhibits that the Zr-MOFs with low CO_2 working capacities (<0.4 mol/kg) are mostly predicted to have relatively close CO_2 working capacities whereas those with medium-high CO_2 working capacities (>1 mol/kg) are located away from the parity line signifying considerable disparities. For instance, PCN-59 with the largest CO_2 working capacity of 3.6 mol/kg (determined with PACMOF charges) is calculated to have a much lower CO_2 working capacity of 0.4 mol/kg using EQeq charges. The bottom left panel compares the CO_2/H_2 selectivities acquired by PACMOF and EQeq charges where most of the structures exhibit comparable selectivities. However, for a number of MOFs, selectivities can differ drastically (PCN-59 with CO_2/H_2 selectivities of 1445.6 (PACMOF based) and 64.9 (EQeq based)). Similarly, the bottom right panel shows a dramatic difference in CO_2 regenerabilities of PCN-59 as it is predicted to exhibit CO_2 regenerabilities of 56.6 and 88.1 % using PACMOF and EQeq charges, respectively. Yet, for the other materials, the differences in CO_2 regenerabilities are mostly negligible as they are very close to the parity line.

3.3. CO_2/N_2 separation

Fig. 5 illustrates the separation performance metrics for the CO_2/N_2 mixture, textural properties of Zr-MOFs and $-\Delta H^{\circ}_{H_2O}$ values. As the colors of the data points in the left panel indicate all structures but one (PCN-59) are highly CO_2 regenerable. While PCN-59 lacks high CO_2 regenerability, it has an unmatched CO_2/N_2 selectivity of 346.0 and CO_2 working capacity of 3.6 mol/kg. The remaining structures exhibit CO_2/N_2 selectivities of 3.6–58.0, CO_2 working capacities of 0.1–2.3 mol/kg, and CO_2 regenerabilities of 83.9–90.6 %. The middle panel demonstrates that the high CO_2/N_2 selectivities (31.3–346.0) are attained by the MOFs with low-medium void fractions (0.345−0.627) whereas the most porous structures (void fraction>0.7) have limited CO_2/N_2 selectivities (3.6–17.3) and CO_2 working capacities (0.1−0.7 mol/kg). For example, the three most CO_2 selective (over N_2) structures (PCN-59, UiO-66-OH, and LIFM-94) possess mediocre void fractions (0.393−0.507) while the least CO_2 selective structure, nitro-MOF, is one of the most porous structures as evidenced by its high void fraction of 0.865. Among the most CO_2 selective (over N_2) Zr-MOFs, UiO-66-CH_3 exhibits the lowest water affinity ($-\Delta H^{\circ}_{H_2O}$ = 14.7 kJ/mol) while PCN-59 has both the highest CO_2/N_2 adsorption selectivity and the highest water affinity as shown in the right panel of Fig. 5.

The left panel of Fig. S7 illustrates the inverse correlation between the CO_2/N_2 selectivity and PLD of the MOFs where the most CO_2 selective (over N_2) structures are located at very small PLD values (<5 Å). Although PCN-59 with the largest CO_2/N_2 selectivity is also located in this region (PLD = 4.28 Å), there are many other structures in the same region which cannot achieve high CO_2/N_2 selectivity. For instance, MOF-525 with one of the lowest PLDs of 4.27 Å acquires a CO_2/N_2 selectivity of only 11.9 hinting the complex interplay of multiple factors instead of a single descriptor such as PLD determining the CO_2/N_2 selectivity. These MOFs' void fractions also vary in a broad range (0.345−0.641) implying a wide array of geometries. Beyond 5 Å, there is still some diversity of void fractions (0.406−0.877), however, not surprisingly, as the PLDs expand, higher void fractions are seen. While the smallest CO_2/N_2 selectivity of 3.6 is predicted for nitro-MOF with one of the largest PLDs of 13.37 Å and void fractions of 0.865, comparably low CO_2/N_2 selectivities may be obtained in MOFs with narrower PLDs (~7.5 Å), yet similar void fractions. The right panel of Fig. S7 portrays the effect of surface area on the CO_2/N_2 selectivity, and it can be concluded that overly large surface areas (>4000 m^2/g) are not beneficial for obtaining high CO_2/N_2 selectivities. For instance, PCN-230 with the largest surface area of 6807.5 m^2/g and a large void fraction of 0.877 attains one of the lowest CO_2/N_2 selectivities of 4.6 which is approached by other MOFs with large surface areas (>4000 m^2/g). In contrast, there is a general increase in CO_2/N_2 selectivities as the surface

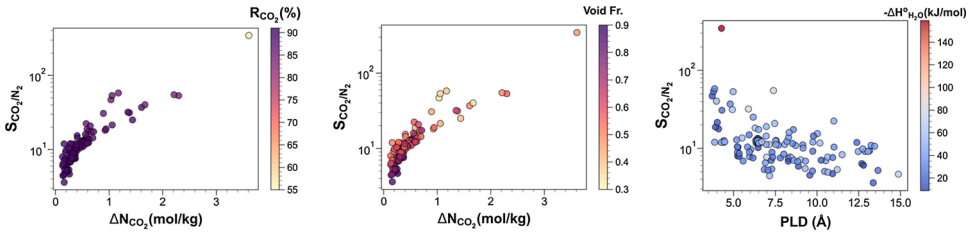


Fig. 5. CO_2/N_2 separation performance metrics in tandem with the void fractions, PLDs and $\Delta H^{\circ}_{H_2O}$ of the Zr-MOFs.

areas diminish, yet it is not a monotonic function as PCN-59 with the largest CO_2/N_2 selectivity of 346.0 lies at 2243.6 m^2/g below which lower CO_2/N_2 selectivities are predicted.

Table 3 lists the top 10 Zr-MOFs for the CO_2/N_2 separation which have PLDs of 3.80–7.39 Å, surface areas of 828.2-3535.7 m^2/g, void fractions of 0.345−0.627, and pore volumes of 0.285-1.047 cm^3/g. Their performance metrics vary in a broad range as evidenced by CO_2/N_2 selectivities of 25.0–346.0, CO_2 working capacities of 1.1–3.6 mol/kg, and CO_2 regenerabilities of 56.3–89.0 %. Amongst them, PCN-59, BUT-10, and LIFM-94 stand out from the rest as the top three materials with CO_2/N_2 selectivities of 346.0, 53.3, and 54.9, CO_2 working capacities of 3.6, 2.3, and 2.2 mol/kg, and CO_2 regenerabilities of 56.3, 84.1, and 83.9 %, successively. Comparing their GCD, PLD, and LCD values, it can be deduced that their pore structures are different from one another. PCN-59, being the top material for CO_2/CO, CO_2/H_2, and CO_2/N_2 separations, is a 12-coordinated Zr-MOF built by a methyl azide involving ligand having fcu topology. Among the top 10 structures, UiO-66-NH_2 possesses the least water affinity ($-\Delta H^{\circ}_{H_2O}$ = 22.4 kJ/mol).

Fig. 6 summarizing the adsorption/separation features (normalized across all materials) of the 10 best performing Zr-MOFs for the CO_2/N_2 separation resembles that of CO_2/H_2 separation except the stronger adsorption of the weakly interacting sorbate (N_2). All materials ranking 2nd-10th adsorb N_2 stronger than the top ranked material, PCN-59, at both adsorption and desorption pressures. As they already exhibit lower CO_2 uptakes than PCN-59, they possess lower separation capability (*i.e.*, CO_2/N_2 selectivity). For instance, BUT-66 acquires the strongest N_2 adsorption at the adsorption condition which severely diminishes its CO_2/N_2 selectivity (~7% of PCN-59). Another observation that can be made is the relatively low CO_2 uptakes of all materials but PCN-59 at the desorption pressure (0.1 bar), ranging between 6–16 % of PCN-59. This hints that if the separation was studied at very low pressures (<0.1 bar), those materials in the shortlist could potentially have limited working capacities. However, as these materials adsorb significant amounts of CO_2 at 1 bar, herein, their CO_2 working capacities are considerably large (within ~30−65 % of PCN-59).

Fig. S8 illustrates the comparisons of gas uptakes, CO_2 working capacities, CO_2/N_2 selectivities, and CO_2 regenerabilities for the CO_2/N_2 separation acquired using PACMOF and EQeq charges. The top left panel depicts that, based on PACMOF and EQeq charges, the CO_2 uptakes can deviate largely while the loadings of weaker interacting N_2 molecules

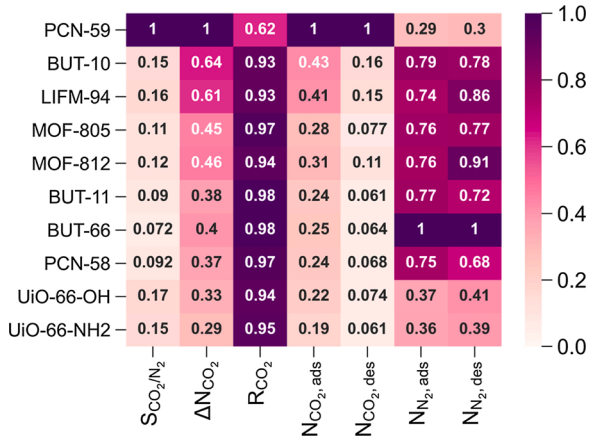


Fig. 6. Normalized adsorption/separation characteristics of the top 10 Zr-MOFs regarding the CO_2/N_2 separation. (In each column, normalization is across all materials.).

are comparable. The top right panel demonstrates the comparison of CO_2 working capacities acquired using PACMOF and EQeq charges. At the low CO_2 working capacity region (<0.4 mol/kg), most of the data points lie very close to the parity line. On the other hand, PCN-59 is predicted to have the largest CO_2 working capacity of 3.6 mol/kg based on PACMOF charges exhibits a much lower CO_2 working capacity of 0.4 mol/kg. Generally, the discrepancies across the predictions based on two partitioning methods are enhanced at high CO_2 working capacity. Selectivity also changes considerably for many MOFs which is reflected in the bottom left panel. For instance, PCN-59 with the highest CO_2/N_2 selectivity of 346.0 based on PACMOF charges is predicted to have more than one order of magnitude smaller CO_2/N_2 selectivity (11.8) based on EQeq charges. The bottom right panel illustrates that most of the materials are predicted to have similar CO_2 regenerabilities based on PACMOF and EQeq charges. The most distinct outlier is PCN-59 with a CO_2 regenerability of 56.3 (87.5) % based on PACMOF (EQeq) charges.

While evaluating the adsorbents based on their selectivity, working capacity, and regenerability is beneficial to understand their potentials, there are also process-related metrics such as productivity which is

Table 3
10 best Zr-MOFs identified (using PACMOF charges) for the separation of CO_2/N_2 together with their structural features.

Structure	SCO_2/N_2	ΔNCO_2 (mol/kg)	RCO_2 (%)	GCD (Å)	PLD (Å)	LCD (Å)	SA (m^2/g)	V_f	V_p (cm^3/g)
PCN-59 [77]	346.0	3.6	56.3	14.50	4.28	14.50	2243.6	0.469	0.652
BUT-10 [78,79]	53.3	2.3	84.1	9.55	4.98	9.55	2452.5	0.581	0.679
LIFM-94 [82]	54.9	2.2	83.9	8.29	7.39	8.29	2190.9	0.507	0.608
MOF-805 [80]	36.9	1.6	88.1	9.23	4.80	9.23	1677.5	0.507	0.489
MOF-812 [80]	40.1	1.7	85.0	5.80	3.97	5.79	939.8	0.345	0.294
BUT-11 [78]	31.3	1.4	89.0	10.25	4.93	10.25	2026.8	0.558	0.616
BUT-66 [81]	25.0	1.4	88.9	6.98	6.18	6.98	1311.7	0.406	0.387
PCN-58 [77]	31.9	1.4	87.6	12.65	5.89	12.65	3535.7	0.627	1.047
UiO-66-OH [83]	58.0	1.2	85.1	7.65	3.87	7.65	872.9	0.393	0.303
UiO-66-NH_2 [84]	53.4	1.1	86.2	7.64	3.80	7.64	828.2	0.365	0.285

shown to correlate well with separation potential (ΔQ) [85]. Table S1 lists the materials rankings as determined using overall separation performance score and separation potential. It can be seen that 9 of 10 top materials are common in both lists suggesting that the overall gas separation performance scores can identify the prospective materials for the real separation process.

3.4. H_2S/CO_2 separation

Fig. 7 delineates the relations between the H_2S/CO_2 separation performance metrics, structural features of the MOFs, and $-\Delta H^{\circ}_{H_2O}$ values. The left panel shows that almost all of the MOFs exhibit H_2S working capacities less than 1.5 mol/kg. The H_2S/CO_2 selectivities of the MOFs range between 2.2 and 109.7 and MOFs' H_2S regenerabilities are predicted to be in a wide range (6.6–91.0 %). The middle panel exhibits that the 5 most H_2S selective MOFs (H_2S/CO_2 selectivity of 80.0–109.7) are moderately or highly porous (void fraction of 0.670−0.780), yet there are other MOFs with similarly high porosities attaining much smaller H_2S/CO_2 selectivities, as low as 2.3. The right panel shows that the 10 most H_2S selective MOFs have medium-high water affinities ($-\Delta H^{\circ}_{H_2O}$ = 57.3–82.5 kJ/mol) where the lowest and highest water affinities belong to Zr-AbBA and NU-1101, respectively.

The left panel of Fig. S9 depicts the complex relationship between the H_2S/CO_2 selectivity and PLD where high H_2S/CO_2 selectivities are not confined to a specific PLD region but rather seen across a broad range of PLD values (~5−15 Å). However, it also shows that quite low H_2S/CO_2 selectivities (~2) can be seen in the same PLD range as well. While many of the highly H_2S selective structures (H_2S/CO_2 selectivity>40) possess high void fractions (>0.7), less H_2S selective structures (H_2S/CO_2 selectivity ~ 2–10) can have both low and high void fractions (0.348−0.865). The right panel of Fig. S9 demonstrates that the most H_2S selective structures are in a broad range of surface areas (~2000−7000 m^2/g). Not surprisingly, among them, those having high surface areas (roughly larger than 4000 m^2/g) also have high void fractions (0.707−0.877). Similar to the S_{H_2S/CO_2} *vs.* PLD case, low H_2S/CO_2 selectivities are observed in a wide range of surface areas (~700−6000 m^2/g).

Table 4 tabulates the 10 best performing Zr-MOFs for the H_2S/CO_2 separation in tandem with their pore characteristics which span PLDs of 5.52–11.21 Å, surface areas of 1708.7-5639.0 m^2/g, void fractions of 0.461−0.840, and pore volumes of 0.501-2.890 cm^3/g. These MOFs exhibit H_2S/CO_2 selectivities of 25.7–109.7, H_2S working capacities of 1.0–2.3 mol/kg, and H_2S regenerabilities of 32.9–84.6 %. The top three MOFs for the H_2S/CO_2 separation are identified as NU-1101, PCN-58, and LMOF-1 exhibiting H_2S/CO_2 selectivities of 109.7, 30.9, and 90.7, H_2S working capacities of 1.6, 2.3, and 1.2 mol/kg, H_2S regenerabilities of 43.0, 56.4, and 43.7 %, successively. They are more porous than many other Zr-MOFs with PLDs of 7.57, 5.89, and 8.47 Å, surface areas of 4783.3, 3535.7, and 4720.1 m^2/g, void fractions of 0.740, 0.627, and 0.780, and pore volumes of 1.652, 1.047, and 1.911 cm^3/g, in successive order. NU-1101 is a 12-coordinated MOF having ftw topology built by a tetratopic organic linker (Py-XP [86]). Among the top 10 materials for H_2S/CO_2 separation, PCN-57 has the lowest water affinity ($-\Delta H^{\circ}_{H_2O}$ = 57.9 kJ/mol) while NU-1101 has the highest ($-\Delta H^{\circ}_{H_2O}$ = 82.5 kJ/mol).

Fig. 8 exhibits the normalized adsorption and separation features of the top 10 Zr-MOFs identified for the H_2S/CO_2 separation. PCN-58, BUT-67, and LIFM-94 stand out from the rest as they adsorb CO_2 stronger than the others. Among them, the first two show considerably lower H_2S/CO_2 selectivity than the others due to the enhanced CO_2 sorption. Although LIFM-94 is one of the cases where CO_2 adsorption is relatively pronounced, its H_2S sorption is also considerably high leading to high H_2S/CO_2 selectivity. While the strong adsorption of H_2S is a benefit in terms of selectivity, as H_2S uptake is high at the desorption conditions as well, LIFM-94 suffers from low H_2S regenerability. Among the top 10 materials, NU-1101 and LMOF-1 are two cases where the H_2S/CO_2 selectivities are the highest as they do not only have the strongest affinity for H_2S but also relatively small CO_2 uptakes. Similar CO_2 uptake is observed in BPHV-MOF where there is a great difference between the adsorption amounts of H_2S at the adsorption and desorption pressures rendering a very high H_2S regenerability. Thus, although its H_2S capture at the adsorption pressure is not as strong as any other MOF in the top 10 list, it ranks as one of the best materials with considerable H_2S working capacity and the largest H_2S regenerability in the top 10 list. This underlines the importance of designing materials which would adsorb insignificant amounts of the desired sorbate at the desorption pressure but adsorb high amounts of sorbate at the adsorption pressure to achieve high working capacity and/or regenerability.

Fig. S10 depicts the comparisons of gas uptakes, H_2S working capacities, H_2S/CO_2 selectivities, and H_2S regenerabilities for the H_2S/CO_2 separation as obtained using PACMOF and EQeq charges. The top left panel describes the highly different gas uptakes that are predicted for both sorbates using PACMOF and EQeq charges. In the top right panel, drastic differences in working capacities can be observed. PCN-58 with the largest H_2S working capacity of 2.3 mol/kg based on PACMOF charges is predicted to have almost zero H_2S working capacity (0.1 mol/kg) based on EQeq charges hinting the great disparities that can be seen across PACMOF and EQeq charges. The comparison of the selectivities based on the charge assignment methods reveals considerable disparities in the bottom left panel. Specifically, H_2S/CO_2 selectivities of LIFM-77 based on PACMOF and EQeq charges are quite different (6.1 *vs.* 42.4). We note that counter examples can also be found where H_2S/CO_2 selectivities based on PACMOF charges are higher than those based on EQeq charges as exemplified by NU-1101 whose H_2S/CO_2 selectivities are predicted to be 109.7 and 3.1 using PACMOF and EQeq charges. Only a small fraction of structures is located around the parity line for selectivity. The bottom right panel demonstrates two wings of data pointing away from the parity line for H_2S regenerability where at the ends of the wings, the disparities become more pronounced. For instance, PCN-59 exhibits a H_2S regenerability of 6.6 (76.2) % based on PACMOF (EQeq) charges whereas LIFM-86 being on the other wing attains a H_2S regenerability of 84.6 (40.4) % utilizing PACMOF (EQeq) charges.

Addressing the question of whether the material rankings are drastically affected by the choice of PACMOF or EQeq method is crucial to guide further experimental and theoretical studies. Fig. 9 depicts the MOF rankings determined using PACMOF and EQeq charges for all gas separations studied. Regarding the CO_2/CO separation, the top left panel shows that many of the low-ranking structures lie in close proximity to the parity line, yet significant differences can be observed for high-

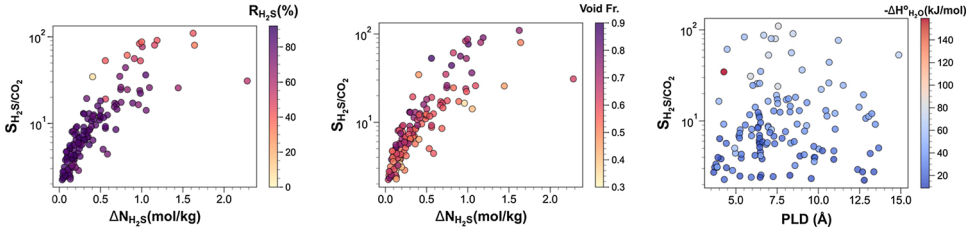


Fig. 7. H_2S/CO_2 separation performance metrics along with the void fractions, PLDs, and $\Delta H^{\circ}_{H_2O}$ of the Zr-MOFs.

Table 4
10 highest performing Zr-MOFs identified (using PACMOF charges) for the separation of H_2S/CO_2 and their structural features.

Structure	S_{H_2S/CO_2}	ΔNH_2S (mol/kg)	RH_2S (%)	GCD (Å)	PLD (Å)	LCD (Å)	SA (m^2/g)	V_f	V_p (cm^3/g)
NU-1101 [86]	109.7	1.6	43.0	18.00	7.57	18.00	4783.3	0.740	1.652
PCN-58 [77]	30.9	2.3	56.4	12.65	5.89	12.65	3535.7	0.627	1.047
LMOF-1 [87]	90.7	1.2	43.7	20.49	8.47	20.49	4720.1	0.780	1.911
LIFM-94 [82]	79.8	1.6	32.9	8.29	7.39	8.29	2190.9	0.507	0.608
PCN-56 [77,88]	80.0	1.2	48.8	16.66	7.14	16.66	4230.5	0.707	1.393
NU-1103 [86]	76.6	1.0	57.6	23.91	11.21	23.91	5639.0	0.840	2.890
BPHV-MOF [89]	36.2	1.0	84.6	14.39	9.02	14.39	4552.2	0.773	1.724
PCN-57 [77]	83.3	1.0	44.5	17.81	5.52	17.76	3864.2	0.670	1.243
ZrDMTD [90]	87.2	1.0	39.8	16.67	6.69	16.67	3892.2	0.707	1.292
BUT-67 [81]	25.7	1.4	63.1	7.96	6.29	7.90	1708.7	0.461	0.501

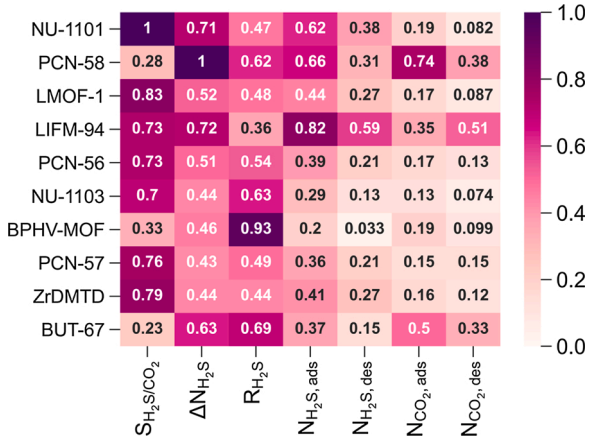


Fig. 8. Normalized adsorption/separation characteristics of the top 10 Zr-MOFs regarding the H_2S/CO_2 separation. (In each column, normalization is across all materials.).

ranking structures. For instance, many structures having high rankings according to EQeq-based results possess much lower rankings when evaluated based on PACMOF charges. As an example, LIFM-32 ranked 5th based on EQeq-based predictions rank only 73rd according to PACMOF-based simulations. Conversely, PCN-58, one of the top materials (3rd) according to PACMOF-based simulations, exhibits a low ranking of 78th based on EQeq charges. Due to such distinct disparities, data points are highly scattered around the parity line for the top-ranked structures identified based on either PACMOF or EQeq charges. Significant material ranking disparities can also be observed for CO_2/H_2 separation (top right panel) as exemplified by BUT-10 with rankings of 2nd and 50th based on PACMOF and EQeq charges. For the material rankings as to the CO_2/N_2 separation, the bottom left panel shows highly scattered data points around the parity line suggesting that significantly different material shortlists would be obtained using PACMOF and EQeq charges. The differences in rankings can be quite drastic as illustrated by PCN-58 having a ranking of 8th based on PACMOF charges while ranked 71st based on EQeq charges. The bottom right panel shows the significant differences in MOF rankings regarding the H_2S/CO_2 separation based on PACMOF and EQeq charges as most of the structures are located far away from the parity line. For instance, NU-1101, PCN-58, and LMOF-1 ranked 1st, 2nd, and 3rd based on PACMOF charges would rank 73rd, 76th, and 75th based on EQeq charges. These examples

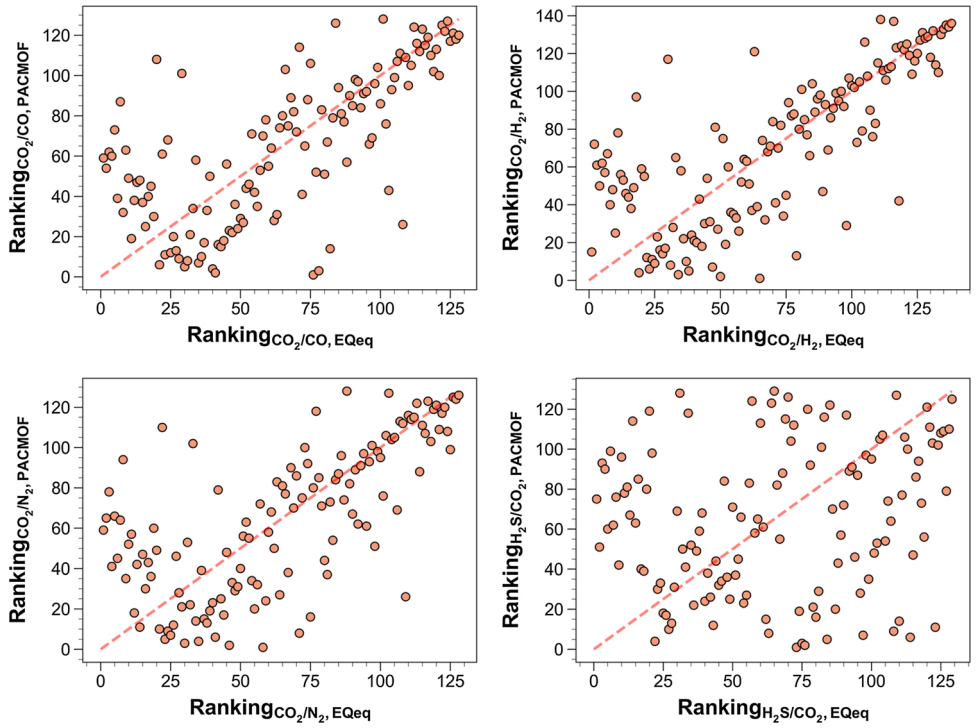


Fig. 9. Comparison of material rankings obtained using PACMOF and EQeq charges for CO_2/CO, CO_2/H_2, CO_2/N_2, and H_2S/CO_2 separation.

clearly show the large extents of differences that can be observed in the material rankings and, thus, top material shortlists. Overall, as there are such large differences in the performance metrics, material rankings using PACMOF and EQeq charges are considerably different in all four separations investigated. It is known that the EQeq charges can significantly deviate from chemically meaningful DDEC charges [68,91], while PACMOF charges can represent the DDEC charges well overall [54]. For instance, in UiO-66, the deviations between PACMOF and DDEC charges for Zr, O, C, and H atoms are much smaller than those between EQeq and DDEC charges implying that the PACMOF charges are chemically more relevant (see Table S2) [92] and the predictions based on PACMOF charges are anticipated to be more accurate.

Besides investigating the gas separation performances of the structures and identifying the best performing materials, it is also crucial to explore the adsorbate density profiles which can reveal various preferred adsorption sites and adsorption mechanisms. The density plots shown in the Figs. S11-S18 for the top three materials identified for each separation demonstrate that the strongly adsorbed gas (CO_2 for CO_2/CO, CO_2/H_2, and CO_2/N_2 mixtures, and H_2S for H_2S/CO_2 mixture) is more localized than the weakly adsorbed gas. The former generally tends to adsorb near the confined edges of the triangle-like pores while the latter has a broader spread across the pores, especially at the adsorption pressures where the presence of weakly adsorbed gases could extend towards the centers of the pores. The interaction energy breakdowns (Fig. S2) show that the strongly adsorbed gas has a much higher host-sorbate interaction energy (larger van-der-Waals and electrostatic interactions) than the weakly adsorbed gas. This suggests that the top MOFs provide highly favorable pore environments for strongly adsorbed gas leading to advantageous confinement and Coulombic effects. In general, it is observed that the strongly adsorbed gas starts experiencing strong interaction around the intersection of multiple linkers at low pressures while the weakly adsorbed gas is relatively more delocalized around the same adsorption sites. However, in H_2S/CO_2 separation, a clear displacement of weakly adsorbed gas by the strongly adsorbed one is observed where H_2S and CO_2 mostly occupy different regions of the pore space in contrast to other gas separations studied where similar regions are occupied. The most distinct example is seen in PCN-58 where H_2S occupies the pore corners while CO_2 can adsorb around the methyl azide group (Figs. S17 and S18). The different list of top materials for H_2S/CO_2 separation in comparison with other gas separations is attributed to the stronger displacements by H_2S and occupation of disparate adsorption sites.

Having investigated separation performances of the Zr-MOFs, we turn to the benchmarking of the presented results with the previous studies. Comparing the CO_2/CO separation performances of the Zr-MOFs with those reported in the literature, it can be concluded that the range of CO_2/CO selectivities in the literature is much broader than that of the Zr-MOFs as the former involves CO selective materials and extremely large CO_2/CO selectivity (12000) [28–30]. Similarly, the previous CO_2/H_2 large-scale screening studies [11,12] identified potentially more CO_2 selective adsorbents than Zr-MOFs. In those two studies [11,12], the CO_2 working capacities of the structures are found to be in the ranges of 0.007–4.60 and 1.62×10^{-3}-7.05 mol/kg implying that some MOF structures may exhibit higher CO_2 working capacities than the Zr-MOFs. For the CO_2/N_2 separation, the Zr-MOFs investigated in this work can outperform some of the structures reported in the literature in terms of CO_2/N_2 selectivity, however, there are also other structures which can be more CO_2 selective than Zr-MOFs [20–22]. Thus, with regard to the CO_2/N_2 selectivity, it can be deduced that the Zr-MOFs would lie in the middle of the spectrum. Looking at the H_2S/CO_2 selectivities, the results presented herein are highly interesting as they significantly outperform MIL-47 and PAF-1 variants investigated earlier [36,35] (H_2S/CO_2 selectivity of 2.2–109.7, 4–6, and 1.5–2.5 for Zr-MOFs, MIL-47 variants, and PAF-1 variants, respectively) at the same adsorption conditions. However, rather than selectivity only, multiple factors ought to be considered for the practical use of adsorbents. As many of the earlier works did not report all three performance metrics calculated in this work, a direct comparison of the structure performances is mostly not possible.

4. Conclusions

In this study, CO_2/CO, CO_2/H_2, CO_2/N_2, and H_2S/CO_2 separation properties of more than 100 Zr-MOF adsorbents are investigated using two sets of GCMC simulations at the room temperature mimicking VSA operation. The best materials for each separation are determined using a combination of adsorption selectivity, working capacity, and regenerability scores of the structures. For the CO_2/CO, CO_2/H_2, and CO_2/N_2 separation, the selectivities of the top 10 materials are comparable except the top material, PCN-59, which can attain several folds of higher selectivities. For the H_2S/CO_2 separation, the top 10 materials possess different combinations of separation performance scores (*i.e.*, some of them excel at selectivity while others are good at working capacity).

Potentially, the atomistic simulations employing different charges may result in dissimilar trends and examining the extents of such differences can help guide future studies on selecting an appropriate charge partitioning method. Investigating the effect of PACMOF and EQeq charges on the separation performance metrics and material rankings, it has been found that the predictions based on these two partitioning methods can deviate largely. As EQeq-based predictions may not describe DDEC-based predictions as good as PACMOF-based predictions for a large number of MOFs [54], our main discussion relies on PACMOF charges. It should be noted that the success of the machine learning model trained to derive PACMOF charges depends on the structures/chemistries involved in the model training. As similar structures were used in the model training, the use of PACMOF charges is considered appropriate for this study. For the forthcoming studies regarding other sets of materials, we think that similar structure/chemistry considerations should be made to evaluate the appropriateness of PACMOF charges.

CRediT authorship contribution statement

Hakan Demir: Conceptualization, Methodology, Software, Validation, Investigation, Writing - original draft, Writing - review & editing. **Seda Keskin:** Conceptualization, Supervision, Methodology, Investigation, Writing - original draft, Writing - review & editing.

Declaration of Competing Interest

The authors declare that they have no known competing financial interests or personal relationships that could have appeared to influence the work reported in this paper.

Acknowledgments

S.K. acknowledges ERC-2017-Starting Grant. This study has received funding from the European Research Council (ERC) under the European Union's Horizon 2020 research and innovation programme (ERC-2017-Starting Grant, grant agreement no. 756489-COSMOS). The numerical calculations reported in this paper were partially performed at TUBITAK ULAKBIM, High Performance and Grid Computing Center (TRUBA resources).

Appendix A. Supplementary data

Supplementary material related to this article can be found, in the online version, at doi:https://doi.org/10.1016/j.jcou.2021.101811.

References

[1] T. Chokbunpiam, S. Fritzsche, V. Parasuk, J. Caro, S. Assabumrungrat, Molecular simulations of a CO2/CO mixture in MIL-127, Chem. Phys. Lett. 696 (2018) 86–91.

[2] K. Munusamy, G. Sethia, D.V. Patil, P.B. Somayajulu Rallapalli, R.S. Somani, H. C. Bajaj, Sorption of carbon dioxide, methane, nitrogen and carbon monoxide on MIL-101(Cr): volumetric measurements and dynamic adsorption studies, Chem. Eng. J. 195–196 (2012) 359–368.

[3] R. Aniruddha, I. Sreedhar, B.M. Reddy, MOFs in carbon capture-past, present and future, J. CO2 Util. 42 (2020) 101297.

[4] Y.G. Chung, D.A. Gómez-Gualdrón, P. Li, K.T. Leperi, P. Deria, H. Zhang, N. A. Vermeulen, J.F. Stoddart, F. You, J.T. Hupp, O.K. Farha, R.Q. Snurr, In silico discovery of metal-organic frameworks for precombustion CO2 capture using a genetic algorithm, Sci. Adv. 2 (10) (2016).

[5] K. Sumida, D.L. Rogow, J.A. Mason, T.M. McDonald, E.D. Bloch, Z.R. Herm, T.-H. Bae, J.R. Long, Carbon dioxide capture in metal–organic frameworks, Chem. Rev. 112 (2) (2012) 724–781.

[6] D. Korelskiy, M. Grahn, P. Ye, M. Zhou, J. Hedlund, A study of CO2/CO separation by sub-micron b-oriented MFI membranes, RSC Adv. 6 (70) (2016) 65475–65482.

[7] T. Pham, K.A. Forrest, B. Space, An unusual H2 sorption mechanism in PCN-14: insights from molecular simulation, Phys. Chem. Chem. Phys. 18 (31) (2016) 21421–21430.

[8] Z.R. Herm, J.A. Swisher, B. Smit, R. Krishna, J.R. Long, Metal−organic frameworks as adsorbents for hydrogen purification and precombustion carbon dioxide capture, J. Am. Chem. Soc. 133 (15) (2011) 5664–5667.

[9] P. García-Holley, B. Schweitzer, T. Islamoglu, Y. Liu, L. Lin, S. Rodriguez, M. H. Weston, J.T. Hupp, D.A. Gómez-Gualdrón, T. Yildirim, O.K. Farha, Benchmark study of hydrogen storage in metal–organic frameworks under temperature and pressure swing conditions, ACS Energy Lett. 3 (3) (2018) 748–754.

[10] Z. Sumer, S. Keskin, Ranking of MOF adsorbents for CO2 separations: a molecular simulation study, Ind. Eng. Chem. Res. 55 (39) (2016) 10404–10419.

[11] G. Avci, S. Velioglu, S. Keskin, High-throughput screening of MOF adsorbents and membranes for H2 purification and CO2 capture, ACS Appl. Mater. Interfaces 10 (39) (2018) 33693–33706.

[12] G. Avci, I. Erucar, S. Keskin, Do new MOFs perform better for CO2 capture and H2 purification? Computational screening of the updated MOF database, ACS Appl. Mater. Interfaces 12 (37) (2020) 41567–41579.

[13] A.L. Myers, J.M. Prausnitz, Thermodynamics of mixed-gas adsorption, AIChE J. 11 (1) (1965) 121–127.

[14] S. Liu, S. Yao, B. Liu, X. Sun, Y. Yuan, G. Li, L. Zhang, Y. Liu, Two ultramicroporous metal–organic frameworks assembled from binuclear secondary building units for highly selective CO2/N2 separation, Dalton Trans. 48 (5) (2019) 1680–1685.

[15] W. Gao, S. Liang, R. Wang, Q. Jiang, Y. Zhang, Q. Zheng, B. Xie, C.Y. Toe, X. Zhu, J. Wang, L. Huang, Y. Gao, Z. Wang, C. Jo, Q. Wang, L. Wang, Y. Liu, B. Louis, J. Scott, A.-C. Roger, R. Amal, H. He, S.-E. Park, Industrial carbon dioxide capture and utilization: state of the art and future challenges, Chem. Soc. Rev. 49 (23) (2020) 8584–8686.

[16] C. Zahasky, S. Krevor, Global geologic carbon storage requirements of climate change mitigation scenarios, Energy Environ. Sci. 13 (6) (2020) 1561–1567.

[17] R.S. Haszeldine, Carbon Capture and Storage: How Green Can Black Be? Science 325 (5948) (2009) 1647–1652.

[18] C. Shi, L. Li, Y. Li, High-throughput screening of hypothetical aluminosilicate zeolites for CO2 capture from flue gas, J. CO2 Util. 42 (2020) 101346.

[19] J. Zhao, S. Deng, L. Zhao, X. Yuan, B. Wang, L. Chen, K. Wu, Synergistic and competitive effect of H2O on CO2 adsorption capture: mechanism explanations based on molecular dynamic simulation, J. CO2 Util. 52 (2021) 101662.

[20] J. Yu, Y. Wu, P.B. Balbuena, Response of metal sites toward water effects on postcombustion CO2 capture in metal–organic frameworks, ACS Sustain. Chem. Eng. 4 (4) (2016) 2387–2394.

[21] H. Cui, Y. Ye, T. Liu, Z.A. Alothman, O. Alduhaish, R.-B. Lin, B. Chen, Isoreticular microporous metal–organic frameworks for carbon dioxide capture, Inorg. Chem. 59 (23) (2020) 17143–17148.

[22] J. Dai, D. Xie, Y. Liu, Z. Zhang, Y. Yang, Q. Yang, Q. Ren, Z. Bao, Supramolecular Metal–Organic Framework for CO2/CH4 and CO2/N2 Separation, Ind. Eng. Chem. Res. 59 (16) (2020) 7866–7874.

[23] P.G. Boyd, A. Chidambaram, E. García-Díez, C.P. Ireland, T.D. Daff, R. Bounds, A. Gładysiak, P. Schouwink, S.M. Moosavi, M.M. Maroto-Valer, J.A. Reimer, J.A. R. Navarro, T.K. Woo, S. Garcia, K.C. Stylianou, B. Smit, Data-driven design of metal–organic frameworks for wet flue gas CO2 capture, Nature 576 (7786) (2019) 253–256.

[24] J.R. Karra, K.S. Walton, Molecular simulations and experimental studies of CO2, CO, and N2 adsorption in metal−organic frameworks, J. Phys. Chem. C 114 (37) (2010) 15735–15740.

[25] D.A. Reed, D.J. Xiao, M.I. Gonzalez, L.E. Darago, Z.R. Herm, F. Grandjean, J. R. Long, Reversible CO scavenging via adsorbate-dependent spin state transitions in an Iron(II)–Triazolate metal–Organic framework, J. Am. Chem. Soc. 138 (17) (2016) 5594–5602.

[26] R.-P. Ye, J. Ding, W. Gong, M.D. Argyle, Q. Zhong, Y. Wang, C.K. Russell, Z. Xu, A. G. Russell, Q. Li, M. Fan, Y.-G. Yao, CO2 hydrogenation to high-value products via heterogeneous catalysis, Nat. Commun. 10 (1) (2019) 5698.

[27] A. Evans, M. Cummings, D. Decarolis, D. Gianolio, S. Shahid, G. Law, M. Attfield, D. Law, C. Petit, Optimisation of Cu+ impregnation of MOF-74 to improve CO/N2 and CO/CO2 separations, RSC Adv. 10 (9) (2020) 5152–5162.

[28] P. Mishra, S. Edubilli, B. Mandal, S. Gumma, Adsorption characteristics of metal–organic frameworks containing coordinatively unsaturated metal sites: effect of metal cations and adsorbate properties, J. Phys. Chem. C 118 (13) (2014) 6847–6855.

[29] H. Kim, M. Sohail, K. Yim, Y.C. Park, D.H. Chun, H.J. Kim, S.O. Han, J.-H. Moon, Effective CO2 and CO separation using [M2(DOBDC)] (M = Mg, Co, Ni) with unsaturated metal sites and excavation of their adsorption sites, ACS Appl. Mater. Interfaces 11 (7) (2019) 7014–7021.

[30] K.-J. Chen, Q.-Y. Yang, S. Sen, D.G. Madden, A. Kumar, T. Pham, K.A. Forrest, N. Hosono, B. Space, S. Kitagawa, M.J. Zaworotko, Efficient CO2 removal for ultra-pure CO production by two hybrid ultramicroporous materials, Angew. Chemie Int. Ed. 57 (13) (2018) 3332–3336.

[31] N. Heymans, S. Vaesen, G. De Weireld, A complete procedure for acidic gas separation by adsorption on MIL-53 (Al), Microporous Mesoporous Mater. 154 (2012) 93–99.

[32] S. Basu, A.L. Khan, A. Cano-Odena, C. Liu, I.F.J. Vankelecom, Membrane-based technologies for biogas separations, Chem. Soc. Rev. 39 (2) (2010) 750–768.

[33] Y. Belmabkhout, P.M. Bhatt, K. Adil, R.S. Pillai, A. Cadiau, A. Shkurenko, G. Maurin, G. Liu, W.J. Koros, M. Eddaoudi, Natural gas upgrading using a fluorinated MOF with tuned H2S and CO2 adsorption selectivity, Nat. Energy 3 (12) (2018) 1059–1066.

[34] J. Liu, Y. Wei, P. Li, Y. Zhao, R. Zou, Selective H2S/CO2 separation by metal–Organic frameworks based on chemical-physical adsorption, J. Phys. Chem. C 121 (24) (2017) 13249–13255.

[35] D. Zhang, X. Jing, D.S. Sholl, S.B. Sinnott, Molecular simulation of capture of sulfur-containing gases by porous aromatic frameworks, J. Phys. Chem. C 122 (32) (2018) 18456–18467.

[36] V. Sokhanvaran, M. Gomar, S. Yeganegi, H2S separation from biogas by adsorption on functionalized MIL-47-X (X = −OH and − OCH3): a simulation study, Appl. Surf. Sci. 479 (2019) 1006–1013.

[37] P.M. Bhatt, Y. Belmabkhout, A.H. Assen, Ł.J. Weseliński, H. Jiang, A. Cadiau, D.-X. Xue, M. Eddaoudi, Isoreticular rare earth fcu-MOFs for the selective removal of H_2S from CO_2 containing gases, Chem. Eng. J. 324 (2017) 392–396.

[38] N. Li, J. Xu, R. Feng, T.-L. Hu, X.-H. Bu, Governing metal–organic frameworks towards high stability, Chem. Commun. 52 (55) (2016) 8501–8513.

[39] S. Yuan, J.-S. Qin, C.T. Lollar, H.-C. Zhou, Stable metal–organic frameworks with group 4 metals: current status and trends, ACS Cent. Sci. 4 (4) (2018) 440–450.

[40] A.J. Howarth, Y. Liu, P. Li, Z. Li, T.C. Wang, J.T. Hupp, O.K. Farha, Chemical, thermal and mechanical stabilities of metal–organic frameworks, Nat. Rev. Mater. 1 (2016) 15018, https://doi.org/10.1038/natrevmats.2015.18.

[41] Y. Bai, Y. Dou, L.-H. Xie, W. Rutledge, J.-R. Li, H.-C. Zhou, Zr-based metal–organic frameworks: design, synthesis, structure, and applications, Chem. Soc. Rev. 45 (8) (2016) 2327–2367.

[42] T. Chen, T.A. Manz, Identifying misbonded atoms in the 2019 CoRE metal–organic framework database, RSC Adv. 10 (45) (2020) 26944–26951.

[43] T.D. Bennett, A.K. Cheetham, A.H. Fuchs, F.-X. Coudert, Interplay between defects, disorder and flexibility in metal-organic frameworks, Nat. Chem. 9 (1) (2017) 11–16.

[44] Y.G. Chung, J. Camp, M. Haranczyk, B.J. Sikora, W. Bury, V. Krungleviciute, T. Yildirim, O.K. Farha, D.S. Sholl, R.Q. Snurr, Computation-ready, experimental metal–organic frameworks: a tool to enable high-throughput screening of nanoporous crystals, Chem. Mater. 26 (21) (2014) 6185–6192.

[45] C. Altintas, G. Avci, H. Daglar, A. Nemati Vesali Azar, I. Erucar, S. Velioglu, S. Keskin, An extensive comparative analysis of two MOF databases: high-throughput screening of computation-ready MOFs for CH4 and H2 adsorption, J. Mater. Chem. A 7 (16) (2019) 9593–9608.

[46] F. Zhou, B. Zheng, D. Liu, Z. Wang, Q. Yang, Large-Scale Structural Refinement and Screening of Zirconium Metal–Organic Frameworks for H2S/CH4 Separation, ACS Appl. Mater. Interfaces 11 (50) (2019) 46984–46992.

[47] E. Haldoupis, S. Nair, D.S. Sholl, Efficient calculation of diffusion limitations in metal organic framework materials: a tool for identifying materials for kinetic separations, J. Am. Chem. Soc. 132 (21) (2010) 7528–7539.

[48] D. Dubbeldam, S. Calero, D.E. Ellis, R.Q. Snurr, RASPA: molecular simulation software for adsorption and diffusion in flexible nanoporous materials, Mol. Simul. 42 (2) (2016) 81–101.

[49] J.J. Potoff, J.I. Siepmann, Vapor–liquid equilibria of mixtures containing alkanes, carbon dioxide, and nitrogen, AIChE J. 47 (7) (2001) 1676–1682.

[50] A. Martín-Calvo, F.D. Lahoz-Martín, S. Calero, Understanding carbon monoxide capture using metal–organic frameworks, J. Phys. Chem. C 116 (11) (2012) 6655–6663.

[51] V. Buch, Path integral simulations of mixed para-D2 and ortho-D2 clusters: the orientational effects, J. Chem. Phys. 100 (10) (1994) 7610–7629.

[52] M.S. Shah, M. Tsapatsis, J.I. Siepmann, Development of the transferable potentials for phase equilibria model for hydrogen sulfide, J. Phys. Chem. B 119 (23) (2015) 7041–7052.

[53] A.K. Rappe, C.J. Casewit, K.S. Colwell, W.A. Goddard, W.M. Skiff, UFF, a full periodic table force field for molecular mechanics and molecular dynamics simulations, J. Am. Chem. Soc. 114 (25) (1992) 10024–10035.

[54] S. Kancharlapalli, A. Gopalan, M. Haranczyk, R.Q. Snurr, Fast and accurate machine learning strategy for calculating partial atomic charges in metal–organic frameworks, J. Chem. Theory Comput. 17 (5) (2021) 3052–3064.

[55] C.E. Wilmer, K.C. Kim, R.Q. Snurr, An extended charge equilibration method, J. Phys. Chem. Lett. 3 (17) (2012) 2506–2511.

[56] T.A. Manz, D.S. Sholl, Chemically meaningful atomic charges that reproduce the electrostatic potential in periodic and nonperiodic materials, J. Chem. Theory Comput. 6 (8) (2010) 2455–2468.

[57] T.A. Manz, D.S. Sholl, Improved atoms-in-Molecule charge partitioning functional for simultaneously reproducing the electrostatic potential and chemical States in

periodic and nonperiodic materials, J. Chem. Theory Comput. 8 (8) (2012) 2844–2867.
[58] T. Watanabe, T.A. Manz, D.S. Sholl, Accurate treatment of Electrostatics during molecular adsorption in nanoporous crystals without assigning point charges to framework atoms, J. Phys. Chem. C. 115 (11) (2011) 4824–4836.
[59] T.A. Manz, Introducing DDEC6 atomic population analysis: part 3. Comprehensive method to compute bond orders, RSC Adv. 7 (72) (2017) 45552–45581.
[60] N.G. Limas, T.A. Manz, Introducing DDEC6 atomic population analysis: part 2. Computed results for a wide range of periodic and nonperiodic materials, RSC Adv. 6 (51) (2016) 45727–45747.
[61] T.A. Manz, N.G. Limas, DDEC6: A Method for Computing Even-Tempered Net Atomic Charges in Periodic and Nonperiodic Materials, arXiv:physics/1512.08270. arXiv.org e-Print archiv, 2015, http://arxiv.org/abs/1512.08270.
[62] T.A. Manz, N.G. Limas, Introducing DDEC6 atomic population analysis: part 1. Charge partitioning theory and methodology, RSC Adv. 6 (53) (2016) 47771–47801.
[63] P.P. Ewald, The calculation of optical and electrostatic grid potential, Ann. Phys. 64 (3) (1921) 253–287.
[64] T.F. Willems, C.H. Rycroft, M. Kazi, J.C. Meza, M. Haranczyk, Algorithms and tools for high-throughput geometry-based analysis of crystalline porous materials, Microporous Mesoporous Mater. 149 (1) (2012) 134–141.
[65] M. Sagastuy-Breña, P.G.M. Mileo, E. Sánchez-González, J.E. Reynolds, T. Jurado-Vázquez, J. Balmaseda, E. González-Zamora, S. Devautour-Vinot, S.M. Humphrey, G. Maurin, I.A. Ibarra, Humidity-induced CO2 capture enhancement in Mg-CUK-1, Dalton Trans. 47 (44) (2018) 15827–15834.
[66] I. Erucar, S. Keskin, Unlocking the effect of H2O on CO2 separation performance of promising MOFs using atomically detailed simulations, Ind. Eng. Chem. Res. 59 (7) (2020) 3141–3152.
[67] H. Demir, S. Keskin, Zr-MOFs for CF4/CH4, CH4/H2, and CH4/N2 separation: towards the goal of discovering stable and effective adsorbents, Mol. Syst. Des. Eng. (2021).
[68] D. Ongari, P.G. Boyd, O. Kadioglu, A.K. Mace, S. Keskin, B. Smit, Evaluating charge equilibration methods to generate electrostatic fields in nanoporous materials, J. Chem. Theory Comput. 15 (1) (2019) 382–401.
[69] A.K. Rappe, W.A. Goddard, Charge equilibration for molecular dynamics simulations, J. Phys. Chem. 95 (8) (1991) 3358–3363.
[70] S. Li, Y.G. Chung, R.Q. Snurr, High-throughput screening of metal–organic frameworks for CO2 capture in the presence of water, Langmuir 32 (40) (2016) 10368–10376.
[71] R. Mercado, B. Vlaisavljevich, L.-C. Lin, K. Lee, Y. Lee, J.A. Mason, D.J. Xiao, M. I. Gonzalez, M.T. Kapelewski, J.B. Neaton, B. Smit, Force field development from periodic density functional theory calculations for gas separation applications using metal–organic frameworks, J. Phys. Chem. C 120 (23) (2016) 12590–12604.
[72] S. Bendt, Y. Dong, F.J. Keil, Diffusion of water and carbon dioxide and mixtures thereof in Mg-MOF-74, J. Phys. Chem. C 123 (13) (2019) 8212–8220.
[73] M. Agrawal, D.S. Sholl, Effects of intrinsic flexibility on adsorption properties of metal–organic frameworks at dilute and nondilute loadings, ACS Appl. Mater. Interfaces 11 (34) (2019) 31060–31068.
[74] M. Witman, S. Ling, S. Jawahery, P.G. Boyd, M. Haranczyk, B. Slater, B. Smit, The influence of intrinsic framework flexibility on adsorption in nanoporous materials, J. Am. Chem. Soc. 139 (15) (2017) 5547–5557.
[75] C. Altintas, G. Avci, H. Daglar, A. Nemati Vesali Azar, S. Velioglu, I. Erucar, S. Keskin, Database for CO2 separation performances of MOFs based on computational materials screening, ACS Appl. Mater. Interfaces. 10 (20) (2018) 17257–17268.
[76] H. Daglar, S. Keskin, Recent advances, opportunities, and challenges in high-throughput computational screening of MOFs for gas separations, Coord. Chem. Rev. 422 (2020), 213470.
[77] H.-L. Jiang, D. Feng, T.-F. Liu, J.-R. Li, H.-C. Zhou, Pore surface engineering with controlled loadings of functional groups via click chemistry in highly stable metal–organic frameworks, J. Am. Chem. Soc. 134 (36) (2012) 14690–14693.
[78] B. Wang, H. Huang, X.-L. Lv, Y. Xie, M. Li, J.-R. Li, Tuning CO2 Selective Adsorption over N2 and CH4 in UiO-67 Analogues through Ligand Functionalization, Inorg. Chem. 53 (17) (2014) 9254–9259.
[79] F. Drache, V. Bon, I. Senkovska, M. Adam, A. Eychmüller, S. Kaskel, Vapochromic luminescence of a zirconium-based metal–organic framework for sensing applications, Eur. J. Inorg. Chem. 27 (2016) (2016) 4483–4489.
[80] H. Furukawa, F. Gándara, Y.-B. Zhang, J. Jiang, W.L. Queen, M.R. Hudson, O. M. Yaghi, Water adsorption in porous metal–organic frameworks and related materials, J. Am. Chem. Soc. 136 (11) (2014) 4369–4381.
[81] L.-H. Xie, X.-M. Liu, T. He, J.-R. Li, Metal-Organic Frameworks for the Capture of Trace Aromatic Volatile Organic Compounds, Chem. 4 (8) (2018) 1911–1927.
[82] C.-X. Chen, Q.-F. Qiu, C.-C. Cao, M. Pan, H.-P. Wang, J.-J. Jiang, Z.-W. Wei, K. Zhu, G. Li, C.-Y. Su, Stepwise engineering of pore environments and enhancement of CO2/R22 adsorption capacity through dynamic spacer installation and functionality modification, Chem. Commun. 53 (83) (2017) 11403–11406.
[83] S. Biswas, P. Van Der Voort, A general strategy for the synthesis of functionalised UiO-66 frameworks: characterisation, stability and CO2 adsorption properties, Eur. J. Inorg. Chem. 12 (2013) (2013) 2154–2160.
[84] C.A. Trickett, K.J. Gagnon, S. Lee, F. Gándara, H.-B. Bürgi, O.M. Yaghi, Definitive molecular level characterization of defects in UiO-66 crystals, Angew. Chemie Int. Ed. 54 (38) (2015) 11162–11167.
[85] R. Krishna, Screening metal–organic frameworks for mixture separations in fixed-bed adsorbers using a combined selectivity/capacity metric, RSC Adv. 7 (57) (2017) 35724–35737.
[86] T.C. Wang, W. Bury, D.A. Gómez-Gualdrón, N.A. Vermeulen, J.E. Mondloch, P. Deria, K. Zhang, P.Z. Moghadam, A.A. Sarjeant, R.Q. Snurr, J.F. Stoddart, J. T. Hupp, O.K. Farha, Ultrahigh surface area zirconium MOFs and insights into the applicability of the BET theory, J. Am. Chem. Soc. 137 (10) (2015) 3585–3591.
[87] R. Zou, X. Ren, F. Huang, Y. Zhao, J. Liu, X. Jing, F. Liao, Y. Wang, J. Lin, R. Zou, J. Sun, A luminescent Zr-based metal–organic framework for sensing/capture of nitrobenzene and high-pressure separation of CH4/C2H6, J. Mater. Chem. A 3 (46) (2015) 23493–23500.
[88] O.V. Gutov, S. Molina, E.C. Escudero-Adán, A. Shafir, Modulation by amino acids: toward superior control in the synthesis of zirconium metal–organic frameworks, Chem. – A Eur. J. 22 (38) (2016) 13582–13587.
[89] K. Manna, T. Zhang, F.X. Greene, W. Lin, Bipyridine- and phenanthroline-based metal–organic frameworks for highly efficient and tandem catalytic organic transformations via directed C–H activation, J. Am. Chem. Soc. 137 (7) (2015) 2665–2673.
[90] B. Gui, K.-K. Yee, Y.-L. Wong, S.-M. Yiu, M. Zeller, C. Wang, Z. Xu, Tackling poison and leach: catalysis by dangling thiol–palladium functions within a porous metal–organic solid, Chem. Commun. 51 (32) (2015) 6917–6920.
[91] D. Nazarian, J.S. Camp, D.S. Sholl, A comprehensive set of high-quality point charges for simulations of metal–organic frameworks, Chem. Mater. 28 (3) (2016) 785–793.
[92] K. Sladekova, C. Campbell, C. Grant, A.J. Fletcher, J.R.B. Gomes, M. Jorge, The effect of atomic point charges on adsorption isotherms of CO2 and water in metal organic frameworks, Adsorption 26 (5) (2020) 663–685.